NANO LETTERS

pubs.acs.org/NanoLett Letter

Large and Pressure-Dependent *c*-Axis Piezoresistivity of Highly Oriented Pyrolytic Graphite near Zero Pressure

Bingjie Wang, Juyao Li, Zheng Fang, Yifan Jiang, Shuo Li, Fangyuan Zhan, Zhaohe Dai, Qing Chen,* and Xianlong Wei*

Cite This: https://doi.org/10.1021/acs.nanolett.4c00687 Read Online

ACCESS | Metrics & More | Article Recommendations | Supporting Information

ABSTRACT: The *c*-axis piezoresistivity is a fundamental and important parameter of graphite, but its value near zero pressure has not been well determined. Herein, a new method for studying the *c*-axis piezoresistivity of van der Waals materials near zero pressure is developed on the basis of *in situ* scanning electron microscopy and finite element simulation. The *c*-axis piezoresistivity of microscale highly oriented pyrolytic graphite (HOPG) is found to show a large value of 5.68×10^{-5} kPa^{-1} near zero pressure and decreases by 2 orders of magnitude to the established value of $\sim 10^{-7}$ kPa^{-1} when the pressure increases to 200 MPa. By modulating the serial tunneling barrier model on the basis of the stacking faults, we describe the *c*-axis electrical transport of HOPG under compression. The large *c*-axis piezoresistivity near zero pressure and its large decrease in magnitude with pressure are attributed to the rapid stiffening of the electromechanical properties under compression.

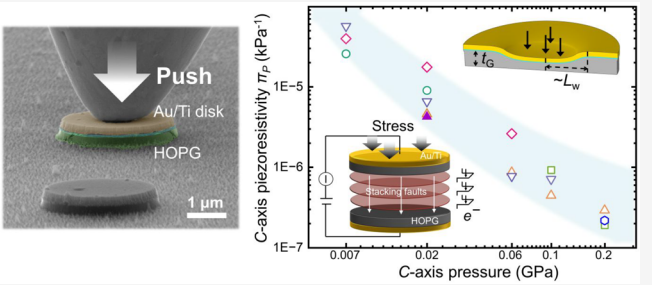

KEYWORDS: *graphite, in situ SEM, c-axis stress, c-axis piezoresistivity, indentation*

Graphite is a typical layered van der Waals material with high structural anisotropy and shows highly anisotropic electrical transport properties with *c*-axis electrical resistivity that is approximately 2−4 orders of magnitude larger than the in-plane resistivity.[1,2] The *c*-axis electrical transport across the van der Waals interacting layers of graphite and its response to the compression pressure are fundamental properties of graphite. Understanding these properties is also helpful for elucidating the *c*-axis electrical transport of graphite and the van der Waals interaction of other layered van der Waals materials. Despite the long and intensive study of graphite, the response of its *c*-axis resistivity to the uniaxial stress at small pressures has not been well determined in experiments, especially near zero pressure.

Previous studies of the piezoresistivity of graphite typically utilized hydrostatic experiments to compress the volume of materials,[3−5] showing that the resistivity decreases nonlinearly with increases in pressure. The typical values of *c*-axis piezoresistivity in the pressure range of 0−5 GPa inferred from the literature are approximately 8.89×10^{-8} to 2.5×10^{-7} kPa^{-1}.[4,6] However, an isotropic hydrostatic experiment is not ideal for measuring *c*-axis piezoresistivity because isotropically applied pressure strongly couples in-plane and out-of-plane deformations[7,8] and larger samples likely contain more defects.[6] The nonlinear piezoresistive response was observed at approximately 1−30 GPa,[5,9] however, the linear *c*-axis piezoresistive response of graphite near zero pressure is still unknown. Some other methods for deforming van der Waals materials may be used to study the piezoresistive response of graphite, including bending,[10,11] wrinkling,[12] forming a microchamber[13] and bubbles,[14,15] etc. However, complex strain fields are introduced as part of those methods. Indention by the conductive probe of the atomic force microscope (AFM) is a straightforward method for studying the *c*-axis piezoresistive properties of van der Waals materials. However, on one hand, the contact mechanics between the AFM probe and tested sample is rather complicated and the actual contact area of the AFM probe is impossible to determine precisely,[16−18] which prevent the determination of the *c*-axis pressure. On the other hand, mechanical loading through a sharp AFM probe may cause highly non-uniform strain[19−22] and potential physical damage to the surface of samples, which are detrimental to the accurate extraction of *c*-axis piezoresistivity. All of the existing methods are therefore not suitable for studying the *c*-axis piezoresistive properties of van der Waals materials under *c*-axis stress, especially near zero pressure.

Received: February 7, 2024
Revised: March 19, 2024
Accepted: March 20, 2024

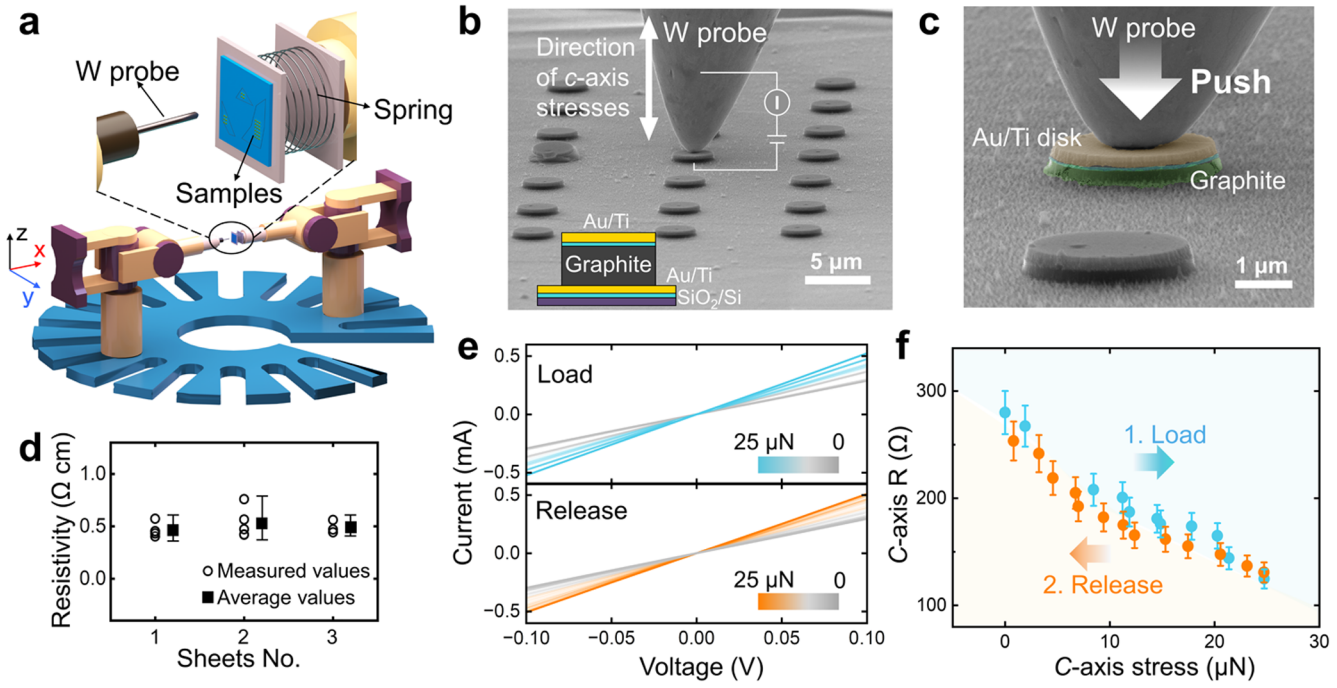

Figure 1. *In situ* piezoresistive measurement of graphite. (a) Schematic drawing of the *in situ* measurement setup. (b) SEM image of graphite islands and their piezoresistive measurement by a tungsten (W) probe. The inset shows the cross-sectional structure of our fabricated graphite islands. (c) Enlarged SEM image showing indentation of graphite by a W probe. The W probe is aligned to the normal of the Au/Ti disk on the top of the graphite island. (d) *c*-Axis resistivity of graphite without *c*-axis pressure measured from the samples fabricated from different graphite sheets. (e) Current−voltage (*I*−*V*) curves of a graphite island under a low bias while subjecting the graphite to *c*-axis stress loading and releasing. (f) *c*-Axis resistance vs *c*-axis stress of the sample as extracted from panel e.

In this work, we develop a method for *in situ* measurement of *c*-axis piezoresistive properties of van der Waals materials under direct uniaxial pressure and study the *c*-axis piezoresistivity of highly oriented pyrolytic graphite (HOPG) near zero pressure. After fabricating micrometer-scale metal/graphite/metal islands on a SiO_2/Si substrate, we achieve *c*-axis uniaxial pressure loading in a fine step of ∼1 MPa and simultaneous *c*-axis resistivity measurement of graphite using an *in situ* scanning electron microscope (SEM) equipped with nanomanipulators. We observe a large *c*-axis piezoresistivity of HOPG up to 5.68×10^{-5}/kPa near zero pressure and a large magnitude decrease from 5.68×10^{-5}/kPa to 1.91×10^{-7}/kPa when the pressure increases from 0 to 200 MPa. The decrease in *c*-axis piezoresistivity is attributed to the stiffening of HOPG under compression.

Our experiments are performed *in situ* inside a SEM equipped with two nanomanipulators. One nanomanipulator was used to hold the tested samples, and the other was used to manipulate a tungsten (W) probe with radii in the range of 100−500 nm. The experimental setup is schematically shown in Figure 1a. The tested samples are connected to a spring that is fixed to the holding nanomanipulator and is used to record the force applied to the tested sample when the spring is indented by the W probe. The force is obtained through the formula $F = kd$, where k is the elastic coefficient of spring and d is the displacement of the substrate, which can be directly measured by SEM images. The elastic coefficient was well calibrated as shown in Figure S1. Our samples for piezoresistive measurements are 3 μm wide circular islands with a metal (200 nm Au/20 nm Ti)/graphite (100−300 nm)/metal (150 nm Au/20 nm Ti) stacked structure fabricated on a SiO_2/Si substrate. Panels b and c of Figure 1 show the SEM images of our samples and piezoresistive measurement of one sample by a W probe. The typical thickness of graphite in our tested samples is 280 nm, as determined by AFM as shown in Figure S2. To measure the piezoresistive response of a metal/graphite/metal island, the W probe is manipulated to indent the island, and its current−voltage (*I*−*V*) curves are simultaneously measured (see Video 1). The resistance of metal/graphite/metal islands is obtained from the linear *I*−*V* curves at a low bias. The details of fabrication of the samples and piezoresistive measurements are available in the experimental section of the Supporting Information.

To ensure the reliability of electrical measurements, we first measured the *c*-axis resistivity of HOPG without applying *c*-axis stress. To measure the *c*-axis resistance of HOPG, we also fabricated comparative samples, which exhibit the same circular shape in the same sizes as the normal samples except without a graphite film sandwiched between metal films. The resistance of comparative samples gives parasitic resistance R_p (including those of the W probe, metal film, probe−metal disk contact, etc.) of the circuit (see Figure S3a). The perfectly linear and symmetric *I*−*V* characteristics prove the good ohmic contact among the W probe, metals, and graphite. After measuring the resistance (R) of the normal samples, we can obtain the *c*-axis resistivity of graphite through the formula $\rho = (R - R_p)S/t_G$, where S is the area of the sample and t_G is the thickness of the graphite film. Figure 1d shows the *c*-axis resistivities of HOPG measured from samples fabricated from three different graphite sheets. One can see that the *c*-axis resistivities are ∼0.49 Ω cm. The good agreement between our measured *c*-axis resistivity and those published in previous

https://doi.org/10.1021/acs.nanolett.4c00687
Nano Lett. XXXX, XXX, XXX−XXX

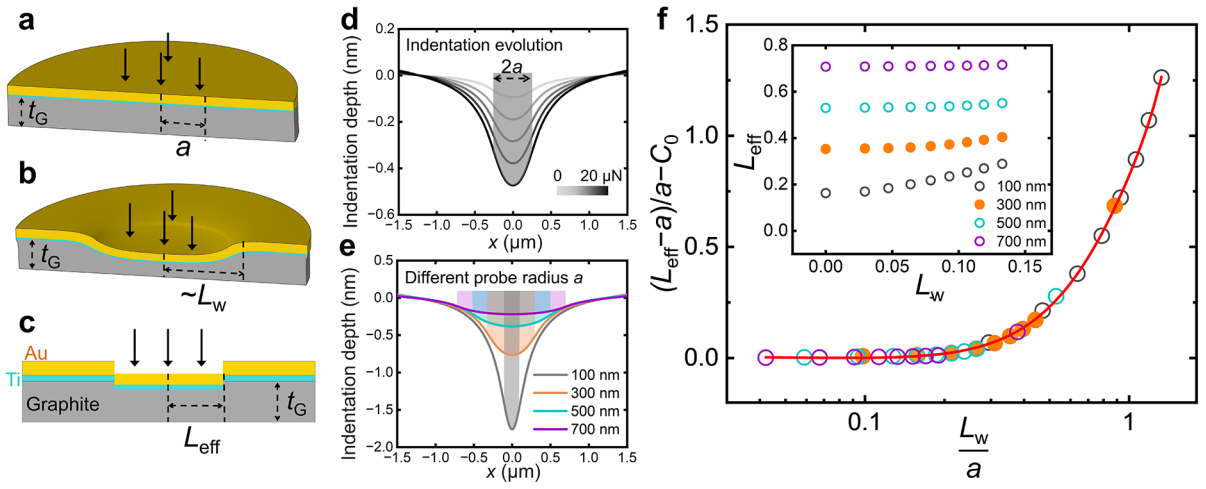

Figure 2. Simulation of indentation by the finite element method (FEM). Schematic diagrams showing the sectional structure of a metal/graphite island (a) before and (b) after indention by a probe. t_G is the thickness of graphite; a is the contact radius of the W probe, and L_W is the horizontal length of the actual indentation. (c) Schematic diagram showing that non-uniform indentation in panel b can be regarded as an equivalent uniform indentation of radius L_{eff}. (d) Indentation profiles of a metal/graphite island subject to various indentation forces F when considering a = 250 nm and Au/Ti disk = 100 nm/20 nm. x represents the radial coordinate. (e) Indentation profiles of a metal/graphite island subject to various contact radii of the W probe (a = 100, 300, 500, and 700 nm) when F = 40 μN. (f) Relationship among equivalent deformation length L_{eff}, Winkler length L_W, and probe radius a. Symbols are results of the FEM, and the solid line is the fitting line with eq 1. The inset shows the dependence of L_{eff} on L_W with different probe radii a.

papers[1,6] indicates the good reliability of our electrical measurements.

The metal/graphite/metal islands are found to exhibit a remarkable piezoresistive response when they are indented by W probes. Figure 1e shows the c-axis transport of a sample when a c-axis force of 25 μN was gradually loaded and released. Linear $I-V$ curves at low bias were observed to show decreases in resistance with an increase in stress. A reversible piezoresistive response was observed during stress loading and releasing. To confirm the origin of the observed piezoresistive response, we performed the same measurements on a comparative sample without a graphite film and no piezoresistive response was observed (see Figure S3b). This indicates that our observed piezoresistive response does come from the graphite film of our samples. Figure 1f shows the c-axis resistances of graphite under different c-axis stresses as extracted from Figure 1e. The graphite sample is found to show an approximately linear decrease of c-axis resistance from 279.9 to 124.7 Ω when a stress of 25 μN is applied.

The precise interpretation of the c-axis piezoresistive response of a graphite sample requires extraction of the c-axis pressure from the applied load. This extraction, however, needs to be considered because the region in which the graphite is compressed is to be determined (Figure 2a,b). There are two natural limits. When the top electrode is highly bendable, the graphite sample would be subject to c-axis deformation, prescribed by the geometry of the W probe. Alternatively, when the top electrode is so thick that it can be considered rigid, the entire graphite sample would be compressed nearly uniformly. The challenge, therefore, comes from the fact that the reality lies between the two limiting cases.

To gain quantitative insights, we perform numerical simulation of this indentation problem using the finite element method (FEM) with the anisotropic properties of graphite considered. It is clear that the graphite sample is deformed not only in the loading region (of radius a, i.e., the contact radius of the W probe) but also over a certain horizontal length L_W as illustrated in Figure 2b. We show the deformation of the graphite sample subject to various indentation forces in Figure 2d and that using different probe radii in Figure 2e. Given the slenderness of the graphite sample, we may use Winkler's mattress model[23] to describe its elastic response so that the stiffness of the mattress is proportional to E_G/t_G, where E_G and t_G are the c-axis modulus and thickness of the graphite sample, respectively. It is then natural to choose the Winkler length to characterize $L_W = (B_{eff}t_G/E_G)^{1/4}$, where B_{eff} is the effective bending stiffness of the Ti/Au disk.

Our simulations have indicated the non-uniform deformation of the graphite under an indentation force F or displacement δ. However, an equivalent deformation length L_{eff} over which the graphite sample is uniformly compressed (see the illustration in Figure 2c) is needed to make the piezoresistive analysis possible. To this end, we apply a mechanical equivalence $F = E_G\epsilon_G A_{eff}$, where $\epsilon_G = \delta/t_G$ and $A_{eff} = \pi L_{eff}^2$, so that L_{eff} can be determined using FEM simulations (more details in Section II of the Supporting Information). This suggests that the non-uniform deformation of the graphite sample over the entire sample size under indentation force F and displacement δ is equivalent to the uniform deformation of the sample over length L_{eff} under the same force and displacement (Figure 2a–c). Apparently, L_{eff} depends on both contact radius a and Winkler length L_W. One can expect that L_{eff} is on the order of the loading probe radius as $L_W \to 0$ and L_{eff} equals the size of the entire graphite sample as $L_W \to \infty$ (i.e., the Ti/Au disk becomes rigid).

Indeed, the inset of Figure 2f shows that L_{eff} increases as L_W or a increases. Interestingly, because there are only three length scales involved so far, we can establish a simple relationship between L_{eff} and the mechanical and geometrical parameters in our systems by

$$\frac{L_{eff}-a}{a} - C_0 \approx -C_1\frac{L_W}{a} + C_2\left(\frac{L_W}{a}\right)^2 - C_3\left(\frac{L_W}{a}\right)^3 \quad (1)$$

https://doi.org/10.1021/acs.nanolett.4c00687
Nano Lett. XXXX, XXX, XXX−XXX

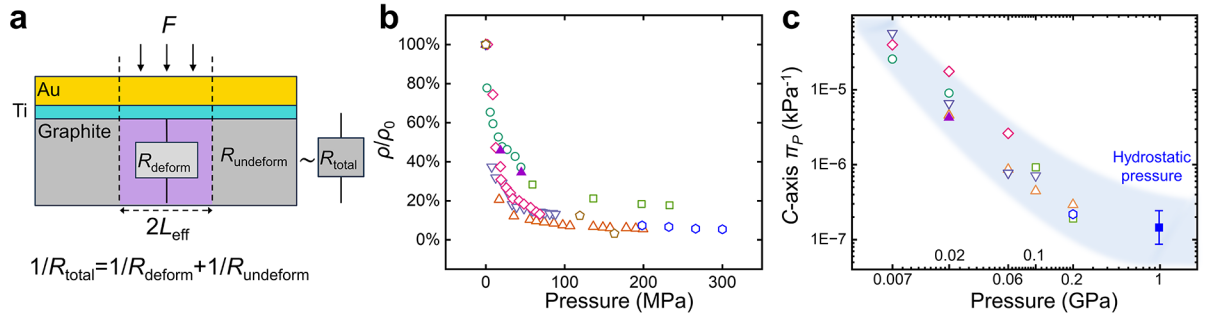

Figure 3. Piezoresistive properties of HOPG samples under *c*-axis stress. (a) Schematic diagram of the *c*-axis resistance of a graphite island under load. R_{deform} ($R_{undeform}$) is the resistance of the central (edge) region under (without) load. R_{total} is the resistance of the whole graphite film. (b) Plots of normalized resistivity vs *c*-axis pressure. Different shapes of marks come from different samples. (c) *c*-Axis piezoresistivity (π_P) of HOPG at different pressure. The same symbols in panels b and c correspond to the data from the same samples. The blue square marked with an error bar shows the data from previous hydrostatic experiments in refs 4 and 6.

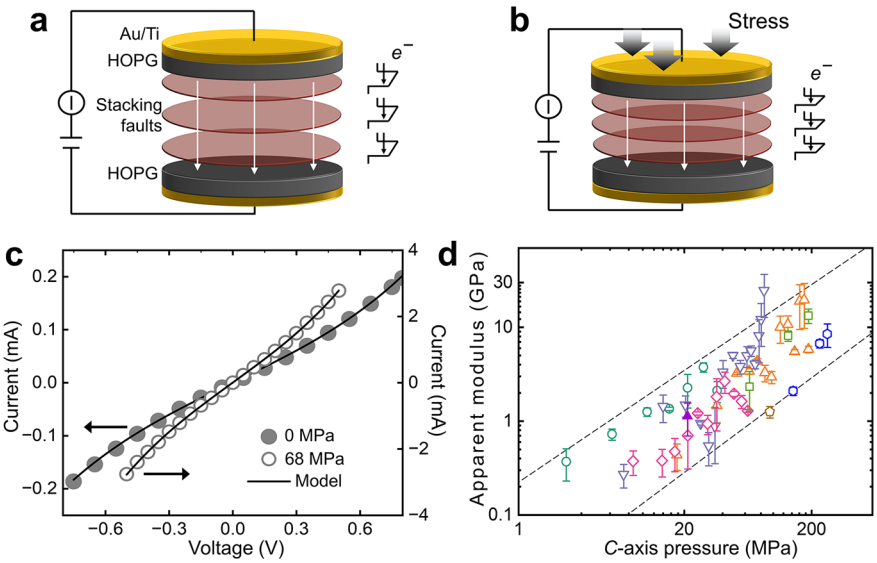

Figure 4. (a) Schematic drawing of the serial tunneling barrier model, in which multiple identical rectangular tunneling barriers are connected in series. (b) Schematic drawing showing the decrease in the width of tunneling barriers under pressure. (c) Nonlinear *I*−*V* characteristics of a sample under 0 and 68 MPa and fittings with the serial tunneling barrier model. (d) *c*-Axis apparent modulus of our samples at different pressures. The data points for different colors come from different samples.

where $C_0 \approx 70$ nm/a − 0.0786, $C_1 \approx 0.159$, $C_2 \approx 1.4720$, and $C_3 \approx 0.489$ are fitting constants based on the simulation results. Figure 2f shows that eq 1 approximates very well for a range of our experimental parameters, including indentation forces, probe radii, electrode thicknesses, graphite thicknesses, etc. This simple relationship also allows us to readily determine L_{eff} for given values of a and B_{eff}, leading to a much more reasonable approximation of the deformation area for piezoresistive analysis than the direct use of either the contact radius of the probe or the radius of the graphite sample (to be shown below). After obtaining L_{eff} for given values of a and B_{eff}, one can obtain the *c*-axis pressure of the tested samples from the applied load.

As the deformation of graphite film under indentation of the probe is equivalent to the uniform deformation in the area with radius L_{eff}, the piezoresistive response observed in Figure 1f is thought to be contributed by the graphite film with radius L_{eff}. The graphite film in our samples is divided into the deformed region (purple area) with radius L_{eff} and the surrounding undeformed region (gray area) as shown in Figure 3a. Due to the anisotropic conductivity of graphite,[1,2] reaching 3.6×10^4, the current will thoroughly extend across the whole cross section and the two regions are considered to be connected in parallel. A sufficiently large graphite sample ensures that bulk contact rather than edge contact dominates.[24] The resistance of the deformed region under pressure can be written as $R_{deform} = R_{total}R_{undeform}/(R_{undeform} - R_{total})$, where R_{total} is the resistance of the whole graphite film as measured in Figure 1f and $R_{undeform}$ is the resistance of the undeformed region. $R_{undeform}$ is obtained from the equation $R_{undeform} = R^0_{total}r^2/(r^2 - L_{eff}^2)$, where R^0_{total} is the resistance of the whole graphite film with zero pressure and r is the radius of the whole graphite film. Neglecting the shrinkage of the graphite thickness, one can write the resistivity of graphite under pressure as $\rho = R_{deform}(\pi L_{eff}^2)/t_G$. Figure 3b shows the normalized *c*-axis resistivity of graphite under different pressures. One can see that the *c*-axis resistivity of graphite decreases fast with pressure at first and then decreases slowly.

In general, if the relationship between resistivity and pressure is linear, piezoresistivity can be directly calculated with the equation $\pi_0 = (d\rho/\rho_0)/P$, where ρ_0 is the resistivity at zero pressure and P is the applied pressure. To fully describe

https://doi.org/10.1021/acs.nanolett.4c00687
Nano Lett. XXXX, XXX, XXX−XXX

the nonlinear *c*-axis piezoresistive response of our samples, we here adopted first-order piezoresistivity π_P at pressure P:

$$\pi_P = -(\mathrm{d}\rho/\mathrm{d}P)/\rho_0 \quad (2)$$

Figure 3c shows the first-order piezoresistivity of different samples at 7, 20, 60, 100, and 200 MPa. As the *c*-axis pressure increases from 0 to 200 MPa, the *c*-axis π_P decreases from 5.68 $\times 10^{-5}$ to 1.91 $\times 10^{-7}$ kPa^{-1}. The values of *c*-axis π_P extracted from previous hydrostatic experiments are included for comparison.[4,6] As the *c*-axis pressure approaches 200 MPa, *c*-axis π_P gradually reproduces the results reported by hydrostatic experiments in the literature. For comparison, π_P values of some common materials, such as III−V, IV−VI group semiconductors and previously reported graphite,[4,6,25−39] are summarized in Figure S4. The obtained *c*-axis piezoresistivity of HOPG present here in a small pressure range (0−20 MPa) is higher than that of most materials reported previously.

The *c*-axis resistivity in HOPG includes a series of hindrances to transport, such as wrinkles, voids, dislocations, impurities, stacking faults, etc.[40−47] Among them, the tunneling barriers induced by stacking faults were reported to dominate the *c*-axis resistivity at room temperature.[46] Because the thickness of our graphite films is much larger than the mean distance between two stacking faults (4−10 nm),[46,47] a serial tunneling barrier model, in which multiple identical rectangular tunneling barriers is connected in series, is assumed to describe the *c*-axis electron transport in our samples as shown in Figure 4a. The effect of pressure on the *c*-axis electron transport is assumed to decrease the width of rectangular tunneling barriers (Figure 4b), that is, the tunnel length. To verify the validity of the model, the general Simmons tunneling formula is adopted to describe $I-V$ curves of our samples (see eq S1 of the Supporting Information).[48,49] Figure 4c shows that the nonlinear $I-V$ curves of a sample both with and without pressure can be well fitted by the general Simmons tunneling formula.

To describe the piezoresistive response of our samples, the Simmons tunneling formula near zero voltage (see eq S2 and Figure S5) is adopted to describe the linear $I-V$ curves at low voltages as shown in Figure 1e.[48,49] It gives the *c*-axis resistance of deformed graphite films under pressure P as

$$R_{\mathrm{deform}} = \frac{8\pi^2\hbar n d_P}{A\beta e^2}\exp(\beta d_P) \quad (3)$$

where d_P is the width of rectangular tunneling barriers under pressure, A is the effective tunneling area, n is the number of stacking faults, and $\beta = 2(2m_c\varphi)^{1/2}/\hbar$ with φ = 4.5 eV being the height of the tunneling barrier,[50−52] $m_c = 12m_e$ being the effective mass of electrons along the *c*-axis,[53,54] and $\hbar$ being the reduced Planck constant. Assuming the shrinkage of tunneling barriers or the interlayer distance of stacking faults is proportional to pressure P with an apparent *c*-axis modulus of E, d_P can be written as $d_P = d_0(1 - P/E)$, where d_0 = 0.34 nm is the width of the tunneling barrier at zero pressure. It should be noted that the apparent modulus here is different from the elastic constant in mechanical measurements and expresses the "hardness" of electromechanical properties obtained by fitting the serial tunneling barrier model. Taking the formula of d_P and $R_{\mathrm{deform}} = \rho t_G/S$ into eq 3, we obtain

$$\frac{\rho}{\rho_0} = \frac{1}{1-\frac{P}{E}}\exp\left(-\frac{\beta d_0 P}{E}\right) \quad (4)$$

Adding the measured resistivity and the corresponding pressure shown in Figure 3b to the equation presented above, we obtained the apparent modulus for different pressures, as shown in Figure 4d. One can see that when the pressure increases to ∼200 MPa, the apparent modulus increases with pressure from <1 to ∼20 GPa, which is a reasonable value for the *c*-axis modulus of HOPG in previous experiments.[20,55−58] The apparent modulus under high pressure is much larger than that near zero pressure, showing a significant stiffening effect in the *c*-axis electromechanical properties. The small apparent modulus near zero pressure and the significant stiffening effect of electromechanical properties are thought to be responsible for our measured large *c*-axis piezoresistivity near zero pressure and its decrease by a large magnitude with pressure.

The much smaller apparent modulus near zero pressure can be attributed to the following. First, as the high pressure on the order of gigapascals applied in hydrostatic experiments induces a nonlinear mechanical response of graphite,[5,59,60] the softening of the elastic modulus near zero pressure compared with that obtained in high-pressure experiments is reasonable. Second, the interlayer distance between some stacking layers in graphite can be larger than that of perfect graphite due to the defects like edge dislocations,[61] interlayer rotation,[62,63] impurities,[64,65] etc. This is thought to result in the softening of interlayer compression at low pressure. Third, while *c*-axis compression is assumed to induce only the shrinkage of rectangular tunneling barriers in our transport model as shown in panels a and b of Figure 4, some other effects of compression may also exist, such as the increase in the effective transport area, reduction of tunneling barriers, etc. The neglect of these effects may also result in a small apparent modulus near zero pressure.

In conclusion, we develop a new method for studying the *c*-axis piezoresistivity of van der Waals materials near zero pressure on the basis of an *in situ* scanning electron microscope and finite element simulation. Upon application of the method, the *c*-axis piezoresistivity of HOPG is studied. Our HOPG samples are found to show a large *c*-axis piezoresistivity of ≤5.68 $\times 10^{-5}$ kPa^{-1} near zero pressure and decreases by 2 orders of magnitude to an established value of ∼10^{-7} kPa^{-1} when the pressure increases to 200 MPa. The decrease in *c*-axis piezoresistivity is attributed to the stiffening of electromechanical properties under compression. The *c*-axis apparent modulus is obtained by describing the *c*-axis electrical transport of HOPG with a serial tunneling barrier model.

■ ASSOCIATED CONTENT

Supporting Information

The Supporting Information is available free of charge at https://pubs.acs.org/doi/10.1021/acs.nanolett.4c00687.

Experimental section, complementary experimental results, including reliability tests, an AFM figure, the tunneling model, and comparison with previous results, and details of finite element analysis and the mechanical model (PDF)

Video of the *in situ* piezoresistive test on graphite (MP4)

https://doi.org/10.1021/acs.nanolett.4c00687
Nano Lett. XXXX, XXX, XXX−XXX

AUTHOR INFORMATION

Corresponding Authors

Qing Chen − *Key Laboratory for the Physics and Chemistry of Nanodevices, School of Electronics, Peking University, Beijing 100871, China;* orcid.org/0000-0002-7919-5159; Email: qingchen@pku.edu.cn

Xianlong Wei − *Key Laboratory for the Physics and Chemistry of Nanodevices, School of Electronics, Peking University, Beijing 100871, China;* orcid.org/0000-0002-1181-9500; Email: weixl@pku.edu.cn

Authors

Bingjie Wang − *Key Laboratory for the Physics and Chemistry of Nanodevices, School of Electronics, Peking University, Beijing 100871, China;* orcid.org/0000-0001-8397-3761

Juyao Li − *Department of Mechanics and Engineering Science, College of Engineering, Peking University, Beijing 100871, China*

Zheng Fang − *Key Laboratory for the Physics and Chemistry of Nanodevices, School of Electronics, Peking University, Beijing 100871, China;* orcid.org/0000-0003-3304-5726

Yifan Jiang − *Key Laboratory for the Physics and Chemistry of Nanodevices, School of Electronics, Peking University, Beijing 100871, China*

Shuo Li − *Key Laboratory for the Physics and Chemistry of Nanodevices, School of Electronics, Peking University, Beijing 100871, China*

Fangyuan Zhan − *Key Laboratory for the Physics and Chemistry of Nanodevices, School of Electronics, Peking University, Beijing 100871, China*

Zhaohe Dai − *Department of Mechanics and Engineering Science, College of Engineering, Peking University, Beijing 100871, China*

Complete contact information is available at: https://pubs.acs.org/10.1021/acs.nanolett.4c00687

Author Contributions

B.W., Z.F., X.W., and Q.C. designed the experiments. B.W. performed *in situ* piezoresistive tests and analyzed experimental data. B.W. and J.L. performed the finite element analyses and used the mechanical model under Z.D.'s supervision. B.W., Y.J., and F.Z. performed sample fabrication. S.L. performed AFM experiments. X.W. and Q.C. supervised the project.

Notes

The authors declare no competing financial interest.

ACKNOWLEDGMENTS

This work was supported by the National Natural Science Foundation of China (Grants 11890671 and 62350040). The authors thank Chong Tian for useful discussions. The authors acknowledge Peking Nanofab for the use of related equipment.

REFERENCES

(1) Matsubara, K.; Sugihara, K.; Tsuzuku, T. Electrical resistance in the c direction of graphite. *Phys. Rev. B* **1990**, *41* (2), 969−974.

(2) Koren, E.; Knoll, A. W.; Lörtscher, E.; Duerig, U. Meso-scale measurement of the electrical spreading resistance in highly anisotropic media. *Appl. Phys. Lett.* **2014**, *105* (12), 123112.

(3) Mao, H.; Bell, P.; Shaner, J. t.; Steinberg, D. J. J. o. a. p. Specific volume measurements of Cu, Mo, Pd, and Ag and calibration of the ruby R 1 fluorescence pressure gauge from 0.06 to 1 Mbar. *J. Appl. Phys.* **1978**, *49* (6), 3276−3283.

(4) Okuyama, N.; Yasunaga, H.; Minomura, S.; Takeya, K. Dependence of the Resistance on Pressure in the c Direction of Pyrolytic and Natural Graphite. *Jpn. J. Appl. Phys.* **1971**, *10* (11), 1645.

(5) Lynch, R. W.; Drickamer, H. G. Effect of high pressure on the lattice parameters of diamond, graphite, and hexagonal boron nitride. *J. Chem. Phys.* **1966**, *44* (1), 181.

(6) Uher, C.; Hockey, R. L.; Benjacob, E. Pressure dependence of the c-axis resistivity of graphite. *Phys. Rev. B* **1987**, *35* (9), 4483−4488.

(7) Huang, S.; Zhang, G.; Fan, F.; Song, C.; Wang, F.; Xing, Q.; Wang, C.; Wu, H.; Yan, H. Strain-tunable van der Waals interactions in few-layer black phosphorus. *Nat. Commun.* **2019**, *10* (1), 2447.

(8) Zhang, L.; Tang, Y.; Khan, A. R.; Hasan, M. M.; Wang, P.; Yan, H.; Yildirim, T.; Torres, J. F.; Neupane, G. P.; Zhang, Y.; Li, Q.; Lu, Y. 2D Materials and Heterostructures at Extreme Pressure. *Adv. Sci.* **2020**, *7* (24), 2002697.

(9) Pimenta Martins, L. G.; Comin, R.; Matos, M. J. S.; Mazzoni, M. S. C.; Neves, B. R. A.; Yankowitz, M. High-pressure studies of atomically thin van der Waals materials. *Appl. Phys. Rev.* **2023**, *10* (1), 011313.

(10) Mohiuddin, T. M. G.; Lombardo, A.; Nair, R. R.; Bonetti, A.; Savini, G.; Jalil, R.; Bonini, N.; Basko, D. M.; Galiotis, C.; Marzari, N.; Novoselov, K. S.; Geim, A. K.; Ferrari, A. C. Uniaxial strain in graphene by Raman spectroscopy: G peak splitting, Gr\"uneisen parameters, and sample orientation. *Phys. Rev. B* **2009**, *79* (20), 205433.

(11) He, K.; Poole, C.; Mak, K. F.; Shan, J. Experimental Demonstration of Continuous Electronic Structure Tuning via Strain in Atomically Thin MoS2. *Nano Lett.* **2013**, *13* (6), 2931−2936.

(12) Castellanos-Gomez, A.; Roldan, R.; Cappelluti, E.; Buscema, M.; Guinea, F.; van der Zant, H. S. J.; Steele, G. A. Local Strain Engineering in Atomically Thin MoS2. *Nano Lett.* **2013**, *13* (11), 5361−5366.

(13) Bunch, J. S.; Verbridge, S. S.; Alden, J. S.; van der Zande, A. M.; Parpia, J. M.; Craighead, H. G.; McEuen, P. L. Impermeable Atomic Membranes from Graphene Sheets. *Nano Lett.* **2008**, *8* (8), 2458−2462.

(14) Ghorbanfekr-Kalashami, H.; Vasu, K. S.; Nair, R. R.; Peeters, F. M.; Neek-Amal, M. Dependence of the shape of graphene nanobubbles on trapped substance. *Nat. Commun.* **2017**, *8*, 15844.

(15) Khestanova, E.; Guinea, F.; Fumagalli, L.; Geim, A. K.; Grigorieva, I. V. Universal shape and pressure inside bubbles appearing in van der Waals heterostructures. *Nat. Commun.* **2016**, *7*, 12587.

(16) Chiou, Y.-C.; Olukan, T. A.; Almahri, M. A.; Apostoleris, H.; Chiu, C. H.; Lai, C.-Y.; Lu, J.-Y.; Santos, S.; Almansouri, I.; Chiesa, M. J. L. Direct Measurement of the Magnitude of the van der Waals Interaction of Single and Multilayer Graphene. *Langmuir* **2018**, *34* (41), 12335−12343.

(17) Rejhon, M.; Lavini, F.; Khosravi, A.; Shestopalov, M.; Kunc, J.; Tosatti, E.; Riedo, E. Relation between interfacial shear and friction force in 2D materials. *Nat. Nanotechnol.* **2022**, *17* (12), 1280−1287.

(18) Mizzi, C. A.; Lin, A. Y. W.; Marks, L. D. Does Flexoelectricity Drive Triboelectricity? *Phys. Rev. Lett.* **2019**, *123* (11), 116103.

(19) Li, X.; Sun, M.; Shan, C.; Chen, Q.; Wei, X. Mechanical Properties of 2D Materials Studied by In Situ Microscopy Techniques. *Adv. Mater. Interfaces* **2018**, *5* (5), 1701246.

(20) Gao, Y.; Kim, S.; Zhou, S.; Chiu, H.-C.; Nélias, D.; Berger, C.; De Heer, W.; Polloni, L.; Sordan, R.; Bongiorno, A.; Riedo, E. Elastic coupling between layers in two-dimensional materials. *Nat. Mater.* **2015**, *14* (7), 714−720.

(21) Kelly, B. T. *Physics of graphite*; Applied Science, 1981.

(22) Park, S. M.; Wang, B.; Chen, L.-Q.; Noh, T. W.; Yang, S. M.; Lee, D. Flexoelectric control of physical properties by atomic force microscopy. *Appl. Phys. Rev.* **2021**, *8* (4), 041327.

(23) Dillard, D. A.; Mukherjee, B.; Karnal, P.; Batra, R. C.; Frechette, J. A review of Winkler's foundation and its profound

influence on adhesion and soft matter applications. *Soft Matter* **2018**, *14* (19), 3669−3683.
(24) Dutta, D.; Oz, A.; Hod, O.; Koren, E. The scaling laws of edge vs. bulk interlayer conduction in mesoscale twisted graphitic interfaces. *Nat. Commun.* **2020**, *11* (1), 4746.
(25) Yeoman, M. L.; Young, D. A. The anisotropic pressure dependence of conduction in well-oriented pyrolytic graphite I. Non-oscillatory effects and the role of carrier-carrier scattering. *J. Phys.: Condens. Matter* **1969**, *2* (10), 1742.
(26) Samara, G. A.; Drickamer, H. G. Effect of Pressure on the Resistance of Fused-Ring Aromatic Compounds. *J. Chem. Phys.* **1962**, *37* (3), 474−479.
(27) Yamamoto, A.; Tsutsumoto, T. Piezoresistive effect of CVD polycrystalline diamond films. *Diamond Relat. Mater.* **2004**, *13* (4−8), 863−866.
(28) Puneetha, P.; Mallem, S. P. R.; Im, K.-S.; An, S.-J.; Lee, D.-Y.; Park, H.; Park, K.-I.; Shim, J. Strain-engineered piezotronic effects in flexible monolayer MoS2 continuous thin films. *Nano Energy* **2022**, *103*, 107863.
(29) Li, X.; Wei, X.; Xu, T.; Pan, D.; Zhao, J.; Chen, Q. Remarkable and Crystal-Structure-Dependent Piezoelectric and Piezoresistive Effects of InAs Nanowires. *Adv. Mater.* **2015**, *27* (18), 2852−2858.
(30) He, R.; Yang, P. Giant piezoresistance effect in silicon nanowires. *Nat. Nanotechnol.* **2006**, *1* (1), 42−46.
(31) Wang, L.; Wu, J.; Shang, M.; Gao, F.; Li, X.; Zheng, Y.; Zhang, D.; Yang, W.; Chen, S. Improved piezoresistive properties of ZnO/SiC nanowire heterojunctions with an optimized piezoelectric nanolayer. *J. Mater. Sci.* **2021**, *56* (30), 17146−17155.
(32) Bridgman, P. W. The Electrical Resistance of Metals under Pressure. *Proc. Am. Acad. Arts Sci.* **1917**, *52* (9), 573−646.
(33) Tang, L.; Mao, Z.; Wang, C.; Fu, Q.; Wang, C.; Zhang, Y.; Shen, J.; Yin, Y.; Shen, B.; Tan, D.; Li, Q.; Wang, Y.; Medhekar, N. V.; Wu, J.; Yuan, H.; Li, Y.; Fuhrer, M. S.; Zheng, C. Giant piezoresistivity in a van der Waals material induced by intralayer atomic motions. *Nat. Commun.* **2023**, *14* (1), 1519.
(34) Cui, J.; Zhang, Z.; Liu, D.; Zhang, D.; Hu, W.; Zou, L.; Lu, Y.; Zhang, C.; Lu, H.; Tang, C.; Jiang, N.; Parkin, I. P.; Guo, D. Unprecedented Piezoresistance Coefficient in Strained Silicon Carbide. *Nano Lett.* **2019**, *19* (9), 6569−6576.
(35) Barlian, A. A.; Park, W. T.; Mallon, J. R.; Rastegar, A. J.; Pruitt, B. L. Review: Semiconductor Piezoresistance for Microsystems. *Proc. IEEE* **2009**, *97* (3), 513−552.
(36) Hollander, L. E.; Vick, G. L.; Diesel, T. J. The Piezoresistive Effect and its Applications. *Rev. Sci. Instrum.* **1960**, *31* (3), 323−327.
(37) Smith, C. J. P. R. Piezoresistance effect in silicon and germanium. *Phys. Rev.* **1954**, *94* (1), 42−49.
(38) Sagar, A. Piezoresistance in n-Type GaAs. *Phys. Rev.* **1958**, *112* (5), 1533−1533.
(39) Rowe, A. C. H. Piezoresistance in silicon and its nanostructures. *J. Mater. Res.* **2014**, *29* (6), 731−744.
(40) Balandin, A. A.; Ghosh, S.; Bao, W.; Calizo, I.; Teweldebrhan, D.; Miao, F.; Lau, C. N. Superior thermal conductivity of single-layer graphene. *Nano Lett.* **2008**, *8* (3), 902−907.
(41) Shin, H.-J.; Kim, K. K.; Benayad, A.; Yoon, S.-M.; Park, H. K.; Jung, I.-S.; Jin, M. H.; Jeong, H.-K.; Kim, J. M.; Choi, J.-Y.; Lee, Y. H. Efficient Reduction of Graphite Oxide by Sodium Borohydride and Its Effect on Electrical Conductance. *Adv. Funct. Mater.* **2009**, *19* (12), 1987−1992.
(42) Yu, A.; Ramesh, P.; Sun, X.; Bekyarova, E.; Itkis, M. E.; Haddon, R. C. Enhanced Thermal Conductivity in a Hybrid Graphite Nanoplatelet - Carbon Nanotube Filler for Epoxy Composites. *Adv. Mater.* **2008**, *20* (24), 4740−4744.
(43) Son, Y.-W.; Cohen, M. L.; Louie, S. G. Half-metallic graphene nanoribbons. *Nature* **2006**, *444* (7117), 347−349.
(44) Slonczewski, J. C.; Weiss, P. R. BAND STRUCTURE OF GRAPHITE. *Phys. Rev.* **1958**, *109* (2), 272−279.
(45) Ono, S. C-axis resistivity of graphite in connection with stacking faults. *J. Phys. Soc. Jpn.* **1976**, *40* (2), 498−504.
(46) Koren, E.; Knoll, A. W.; Loertscher, E.; Duerig, U. Direct experimental observation of stacking fault scattering in highly oriented pyrolytic graphite meso-structures. *Nat. Commun.* **2014**, *5*, 5837.
(47) Maslov, D. L.; Yudson, V. I.; Somoza, A. M.; Ortuño, M. Delocalization by Disorder in Layered Systems. *Phys. Rev. Lett.* **2009**, *102* (21), 216601.
(48) Matthews, N.; Hagmann, M. J.; Mayer, A. Comment:"Generalized formula for the electric tunnel effect between similar electrodes separated by a thin insulating film"[J. Appl. Phys. 34, 1793 (1963)]. *J. Appl. Phys.* **2018**, *123* (13), 1793.
(49) Simmons, J. G. Generalized formula for the electric tunnel effect between similar electrodes separated by a thin insulating film. *J. Appl. Phys.* **1963**, *34* (6), 1793−1803.
(50) Wilder, J. W. G.; Venema, L. C.; Rinzler, A. G.; Smalley, R. E.; Dekker, C. Electronic structure of atomically resolved carbon nanotubes. *Nature* **1998**, *391* (6662), 59−62.
(51) Lan, Y.-W.; Chang, W.-H.; Li, Y.-Y.; Chang, Y.-C.; Chang, C.-S.; Chen, C.-D. Stacking fault induced tunnel barrier in platelet graphite nanofiber. *Appl. Phys. Lett.* **2014**, *105* (10), 103505.
(52) Venugopal, G.; Jung, M. H.; Suemitsu, M.; Kim, S. J. Fabrication of nanoscale three-dimensional graphite stacked-junctions by focused-ion-beam and observation of anomalous transport characteristics. *Carbon* **2011**, *49* (8), 2766−2772.
(53) McClure, J. W. Band Structure of Graphite and de Haas-van Alphen Effect. *Phys. Rev.* **1957**, *108* (3), 612−618.
(54) Soule, D. E. Change in Fermi Surfaces of Graphite by Dilute Acceptor Doping. *IBM J. Res. Dev.* **1964**, *8* (3), 268−273.
(55) Xiao, J.; Zhang, L.; Zhou, K.; Li, J.; Xie, X.; Li, Z. Anisotropic friction behaviour of highly oriented pyrolytic graphite. *Carbon* **2013**, *65*, 53−62.
(56) Li, J.; Gao, T.; Luo, J. Superlubricity of Graphite Induced by Multiple Transferred Graphene Nanoflakes. *Adv. Sci.* **2018**, *5* (3), 1700616.
(57) Rydberg, H.; Dion, M.; Jacobson, N.; Schröder, E.; Hyldgaard, P.; Simak, S.; Langreth, D. C.; Lundqvist, B. I. J. P. r. l. Van der Waals density functional for layered structures. *Phys. Rev. Lett.* **2003**, *91* (12), 126402.
(58) Fang, Z.; Dai, Z.; Wang, B.; Tian, Z.; Yu, C.; Chen, Q.; Wei, X. J. N. L. Pull-to-Peel of Two-Dimensional Materials for the Simultaneous Determination of Elasticity and Adhesion. *Nano Lett.* **2023**, *23* (2), 742−749.
(59) Jansen, H. J. F.; Freeman, A. J. Structural and electronic properties of graphite via an all-electron total-energy local-density approach. *Phys. Rev. B* **1987**, *35* (15), 8207−8214.
(60) Kozioł, Z.; Gawlik, G.; Jagielski, J. Van der Waals interlayer potential of graphitic structures: From Lennard−Jones to Kolmogorov−Crespy and Lebedeva models. *Chin. Phys. B* **2019**, *28* (9), 096101.
(61) McHugh, J. G.; Mouratidis, P.; Impellizzeri, A.; Jolley, K.; Erbahar, D.; Ewels, C. P. Prismatic edge dislocations in graphite. *Carbon* **2022**, *188*, 401−419.
(62) Campanera, J. M.; Savini, G.; Suarez-Martinez, I.; Heggie, M. I. Density functional calculations on the intricacies of Moir\'e patterns on graphite. *Phys. Rev. B* **2007**, *75* (23), 235449.
(63) van Wijk, M. M.; Schuring, A.; Katsnelson, M.; Fasolino, A. Relaxation of moiré patterns for slightly misaligned identical lattices: graphene on graphite. *2D Mater.* **2015**, *2* (3), 034010.
(64) Alliata, D.; Kötz, R.; Haas, O.; Siegenthaler, H. In Situ AFM Study of Interlayer Spacing during Anion Intercalation into HOPG in Aqueous Electrolyte. *Langmuir* **1999**, *15* (24), 8483−8489.
(65) Wang, J.; Sorescu, D. C.; Jeon, S.; Belianinov, A.; Kalinin, S. V.; Baddorf, A. P.; Maksymovych, P. Atomic intercalation to measure adhesion of graphene on graphite. *Nat. Commun.* **2016**, *7* (1), 13263.

https://doi.org/10.1021/acs.nanolett.4c00687
Nano Lett. XXXX, XXX, XXX−XXX